Single-Dislocation Phonons: Atomic-Scale Measurement and Their Thermal Properties

Yue-Hui Li(李跃辉)[1,2†], Bo Han(韩博)[1,2†], Xiao-Long Yang(杨小龙)[3†], Rui-Lin Mao(毛瑞麟)[1,2†*], Fa-Chen Liu(刘法辰)[1,2], Ruo-Chen Shi(时若晨)[1,2], Rui-Shi Qi(亓瑞时)[2], Xiao-Rui Hao(郝小锐)[2], Ning Li(李宁)[2], Bing-Yao Liu(刘秉尧)[2], Xiao-Mei Li(李晓梅)[4], Jin-Long Du(杜进隆)[2*], Ji Chen(陈基)[5,6,7], Wu Li(李武)[8*], and Peng Gao(高鹏)[1,2,6,7*]

[1]*International Center for Quantum Materials, School of Physics, Peking University, Beijing 100871, China*
[2]*Electron Microscopy Laboratory, School of Physics, Peking University, Beijing 100871, China*
[3]*College of Physics, Center of Quantum Materials and Devices, Chongqing University, Chongqing 401331, China*
[4]*School of Integrated Circuits, East China Normal University, Shanghai 200241, China*
[5]*Institute of Condensed Matter and Material Physics, School of Physics, Peking University, Beijing 100871, China*
[6]*Interdisciplinary Institute of Light-Element Quantum Materials and Research Center for Light-Element Advanced Materials, Peking University, Beijing 100871, China*
[7]*Collaborative Innovation Centre of Quantum Matter, Beijing 100871, China*
[8]*Eastern Institute for Advanced Study, Eastern Institute of Technology, Ningbo 315200, China*

(Received 16 March 2025; accepted manuscript online 9 May 2025)

Nanoscale defects such as dislocations have a significant impact on the phonon thermal transport properties in non-metallic materials. To unravel these effects, an understanding of defect phonon modes is essential. Herein, at the atomic scale, the localized phonons of individual dislocations at a Si/Ge interface are measured via monochromated electron energy loss spectroscopy in a scanning transmission electron microscope. These modes are then correlated with the local microstructure, further revealing the dislocation effects on the local thermal transport properties. The dislocation causes a phonon redshift of several milli-electron-volts within about two to four nanometers of the core, where both the strain field and Ge segregation play roles. With the presence of dislocation, the local interfacial thermal conductance can be either enhanced or reduced, depending on the complex interaction and competition between lattice disorder (dislocation) and element disorder (heterointerface mixing and Ge-segregation) at the interface. These findings provide valuable insights to improve the thermal properties of thermoelectric generators and thermal management systems through proper defect engineering.

DOI: 10.1088/0256-307X/42/6/066302 CSTR: 32039.14.0256-307X.42.6.066302

1. Introduction. The atomic-scale and nanoscale lattice imperfections such as heterointerfaces, grain boundaries, and dislocations usually have unique phonon scattering behaviors different from the bulk matrix and thus a significant impact on thermal properties[1,2] in the non-metallic systems such as thermal management materials[3,4] and thermoelectric devices.[5,6] Therefore, probing the local phonon modes and scattering behavior at these imperfections/interfaces is the key to understanding the underlying physics of their thermal properties [e.g., interfacial thermal conductance (ITC)[7]] and subsequently gaining insights into the optimization. Indeed, numerous strategies have been reported to tune the ITC by introducing an intermediate matching layer,[8] ion irradiation,[9,10] dislocations,[11,12] and so on. For example, dislocations are generally considered to increase local thermal resistance. The underlying mechanism lies in that local lattice disorder at dislocations induced by translation symmetry breaking — which refers to deviations from an ideal crystalline arrangement, encompassing point defects (e.g., vacancies), line defects (e.g., dislocations), and planar defects (e.g., stacking faults) — can strongly scatter the bulk phonons, thereby reducing the phonon lifetime. Previous studies reported that dislocations can almost reduce the ITC by half across the GaSb/GaAs interface.[11] Dislocations within grain boundaries of PbSe significantly enhance phonon scattering, thereby leading to a remarkably improved thermoelectric performance.[13] The lattice strain fluctuations induced by in-grain dislocations notably broaden the phonon dispersion and substantially reduce the ITC, thus enabling an extraordinary figure of merit of ∼2.5 in PbTe alloys.[14] However, in addition to lattice disorder, element disorder also usually exists at the dislocation even at the sub-nanometer scale.[15] Element disorder denotes a non-ideal state of random or uneven atomic distribution in materials, manifesting as random lattice substitution (e.g., irregular atomic site occupancy in solid solutions), segregation (local atomic clustering),

†These authors contributed equally to this work.
*Corresponding author. Email: ruilinmao@stu.pku.edu.cn; jldu@pku.edu.cn; wu.li.phys2011@gmail.com; pgao@pku.edu.cn
© 2025 Chinese Physical Society and IOP Publishing Ltd. All rights, including for text and data mining, AI training, and similar technologies, are reserved.

vacancies, or compositional fluctuations—ultimately leading to a loss of periodicity in nanometer-to-atomic-scale composition. Such element-disorder should also play an important role in interfacial thermal transport; for example, a higher ITC across the Al/Si interface can be achieved after ion irradiation due to the ion mixing of the native oxide and silicon.[10] Therefore, the defects in practical materials with multiple disorders can influence the local thermal transport properties in a very complicated manner due to the competition among multiple factors. Revealing such information is highly desirable.

However, most of the previous works on ITC are based on either theoretical calculations or macroscale thermal transport experiments. To accurately understand the effects of defects on phonon transport properties, information about local phonon modes associated with the specific lattice structure and atomic arrangement of individual defects is required. In this work, we combine scanning transmission electron microscopy (STEM), electron energy loss spectroscopy (EELS), and molecular dynamics (MD) simulations to investigate the localized phonon modes of individual dislocations at a Si/Ge interface. The recent progress in EELS equipped with a monochromator in an aberration-corrected STEM has made it possible to measure localized vibrational spectra at nanoscale and atomic scale[16–26] and even correlate the localized defect phonons with thermal transport properties.[27–29] For example, recent works reported that the grain boundaries of silicon,[30] $SrTiO_3$,[31] and Al_2O_3[32] significantly change the local phonon density of states (PhDOS). Meanwhile, the distribution of strain and elements can be simultaneously obtained through quantitatively determining the local atomic arrangement under the STEM studies. The chosen system, Si/Ge alloy, is an excellent thermoelectric material with wide applications in thermoelectric generators converting heat flows into usable electrical energy[33,34] and thermoelectric microrefrigerators providing large cooling power densities,[35] e.g., the thermal energy of radioactive heat sources.[36] Several methods have been proposed to engineer the thermoelectric properties of SiGe alloys, such as nanostructured SiGe alloys,[37] SiGe/Si superlattices,[38] defects,[39] etc. However, the localized phonons of the dislocation in the Si-Ge alloy system and their effects on the thermal transport properties are still largely unknown.

We find that the interface dislocation strongly alters the local phonon modes and thermal conductance. Within about four nanometers of the dislocation core, localized phonon modes exhibit a redshift of several milli-electronvolts (lower than bulk Si and Ge phonon energies), stemming from combined strain fields and elemental segregation. Specifically, tensile strain at the Ge side drives phonon redshift, whereas Ge segregation at the dislocation core dominates phonon softening at the Si side. Although it is widely recognized that the lattice disorder in single crystals decreases the thermal conductance, the effects of dislocation at the Si/Ge interface on thermal transport are surprisingly complex—arising from the interplay and competition between the lattice disorder (discontinuous lattice structure) and element disorder (heterointerface mixing and Ge segregation) mechanisms. Our findings indicate that depending on the elemental segregation, the local ITC around the dislocation can be either enhanced or reduced. For an atomically sharp heterointerface, where substantial phonon energy mismatches exist, the lattice disorder induced by dislocations effectively bridges the PhDOS between the two materials, enhancing PhDOS overlap. Conversely, as the segregation and interdiffusion increase, the system evolves toward a quasi-homogeneous, single-crystal-like state: phonon energy disparities at the interface diminish, reducing the heterointerface's contribution to thermal resistance, while the role of dislocation-associated lattice disorder becomes dominant. In our case, pronounced Ge segregation in the dislocation core leads to ITC degradation akin to single crystal systems, where dislocation-induced phonon scattering becomes the primary resistance mechanism. Our study unveils the localized phonon modes of individual dislocations within complex mechanical-chemical environments, offering critical insights for designing advanced devices with tailored thermal properties via proper dislocation engineering.

2. Atomic Structure and EELS Near the Dislocation. Figure 1(a) shows an atomically resolved high-angle annular dark-field image of a Si/Ge heterojunction interface. The lattice constant of Ge, $d_{\mathrm{Ge}} = 5.66\,\text{Å}$, is approximately 4% larger than that of Si, $d_{\mathrm{Si}} = 5.43\,\text{Å}$, leading to the formation of misfit edge dislocations at the interface as shown in Fig. 1(b). Based on the element distribution maps from core-loss EELS measurement in the Fig. 1(c), Fig. S1 in Supplementary Materials (SM), and the Z-contrast in Fig. 1(b), the element interdiffusion between Ge and Si occurs to form a disordered SiGe mixing layer with a thickness of about two nanometers at the dislocation-free interface, while significant Ge segregation takes place at the dislocation core region.

Figure 1(d) shows the acquired EELS in bulk Si, bulk Ge, the interfacial mixing layer at a dislocation-free region, and the interfacial dislocation core by using off-axis geometry measurement,[40] which is beneficial for enhancing the signal to zero loss peak (ZLP) ratio, especially for the low energy phonons (see Fig. S2 of SM). The spectra are averaged from a spatially resolved map with the standard errors. The details of data processing are shown in Sec. 5 and Fig. S3 in SM. In order to identify the spectral features and correlate them with vibrational modes, the projected phonon density of states (PPDOS) and phonon dispersion were calculated and shown in Fig. 1(e) and Fig. S4 of SM based on density functional perturbation theory (DFPT) (see details in Sec. 5). The calculated phonon modes are in good agreement with those in a previous study.[41] To simplify the description of experimental data, the peaks of phonon spectra are classified into three branches, labeled as α (arrows without a tail), β (arrows with a tail), and γ. According to the calculated PhDOS and phonon dispersion of Si and Ge, α, β, and γ are mainly assigned to transverse acoustic (Si-TA) mode, longitudinal acoustic/optical (Si-LAO) mode, and transverse optical (Si-LO/TO) mode in Si side, respectively. In the Ge layer, α and β are assigned

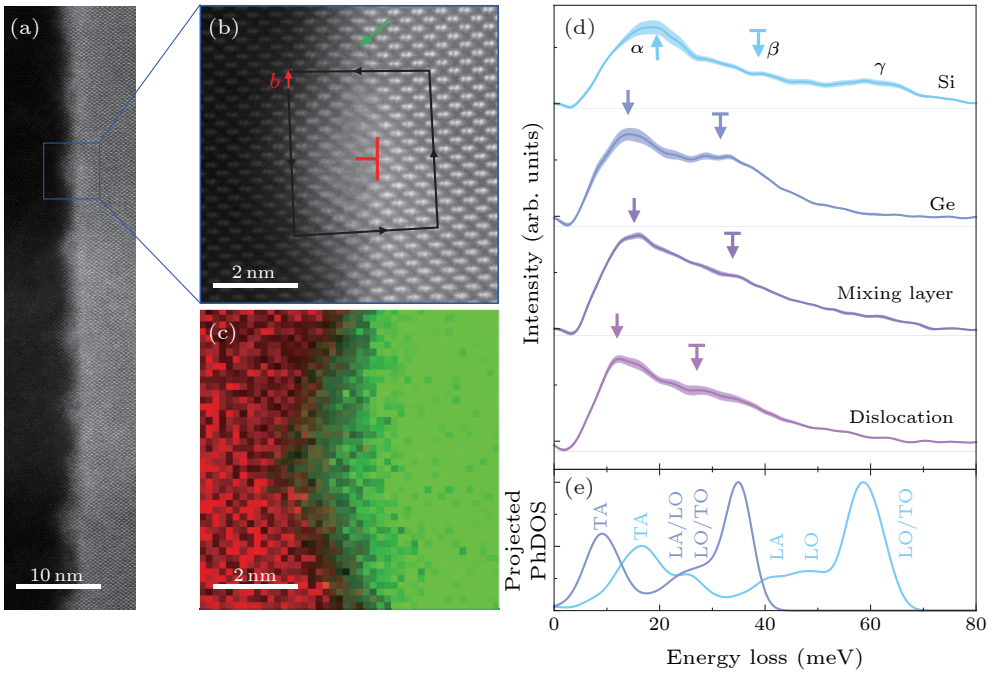

Fig. 1. HAADF image and EELS acquired at different locations. (a) A HAADF image of a Si/Ge interface. (b) An enlarged view showing the atomic structure of an interface dislocation. The Burgers vector $\boldsymbol{b}$ is denoted by the red arrow. The green arrow denotes the disordered mixing layer at the dislocation-free interface region based on the Z-contrast. (c) Element distribution of Si (red) and Ge (green) at the dislocation extracted from EELS of Si-K edge and Ge-K edge. (d) EELS with standard error acquired at different locations. The arrows without (with) tail denote α (β) peaks. The peak assignment is conducted by combing spectroscopic features with theoretical simulation results. The error bar is defined by the standard deviations between binned 5×5 pixels on different places of the sample. The spectrum was normalized by its integral before ZLP subtraction. (e) Calculated phonon PhDOS projected on [110] plane of Si (bule) and Ge (purple).

to Ge-TA mode and Ge-AO (LA, LO, and TO all contribute) mode, respectively. Since the Si-LO/TO phonon is pronounced only in the Si layer, γ is absent in the Ge layer. At the dislocation-free interface region, the α and β peaks are between those in bulk Si and bulk Ge due to element interdiffusion and/or heterointerface phonon modes,[23] while at the dislocation core they have lower energy than either of them (i.e., redshift), indicating the generation of new localized defect modes with different phonon energy.

3. Localization and Redshift Feature of the Dislocation Phonons. Figure 2(a) shows energy-filtered EELS intensity maps of window 6–14 meV, in which the phonon spectrum should be mainly attributed to the dislocation based on Fig. 1(d). It can be observed that the integrated intensity is concentrated at the dislocation core, further verifying the redshift of the α-peak at the dislocation. To quantitatively validate these spectral features, the background-subtracted EELS was fitted using a simple Gaussian peak fitting model. The data processing details are included in Sec. 5. The energy distribution maps of α, β, and γ phonon branches are shown in Figs. 2(b)–2(d), respectively. Notably, near the dislocation core, all three phonon branches show redshift. In contrast, at the dislocation-free interfacial region, the phonon energies of α and β modes gradually transform from Si on the left to Ge on the right, which act as phonon bridges to connect significantly different energies of phonons.[29,42] Specifically, figure 2(e) shows the extracted line profiles of α, β, and γ phonon energy through the interface dislocation (red) and dislocation-free region (black) perpendicular to the interface denoted by the solid rectangles in Fig. 2(a), where all of the dislocation-induced localized modes, α_{disl}, β_{disl}, and γ_{disl} modes show redshift at the dislocation core (labeled as 0 nm). The energy of the α_{disl} mode is ∼1.2 meV lower than that of bulk Ge-TA mode, the energy of the β_{disl} mode is ∼3.1 meV lower than that of the bulk Ge-AO mode, and the energy of γ_{disl} mode is ∼2.3 meV lower than that of the regular interface mode. Figure 2(f) shows the phonon energy changes of α, β, and γ modes through the dislocation core along the interface of the full acquisition area denoted by the rectangles in Fig. S5 of the SM. Therefore, the interfacial dislocation has very different localized phonon modes than the dislocation-free region, implying its important influence on the thermal transport properties. The corresponding Gaussian fitted line profiles have a full width at half maximum of ∼2.5 nm for α_{disl}, ∼3.2 nm for β_{disl}, and ∼4.4 nm for γ_{disl}, respectively, indicating the highly localized nature of the dislocation phonon modes. In fact, due to the possible collection of dipole signals, the Umklapp processes,[43] and the de-channeling effects,[44] the estimated delocalization range of dislocation signals by using large convergence may be slightly exaggerated, i.e., the true physical ranges of dislocation phonons are even smaller. Moreover, the width of the low energy phonon α is the smallest, likely due to the impact nature of acoustic

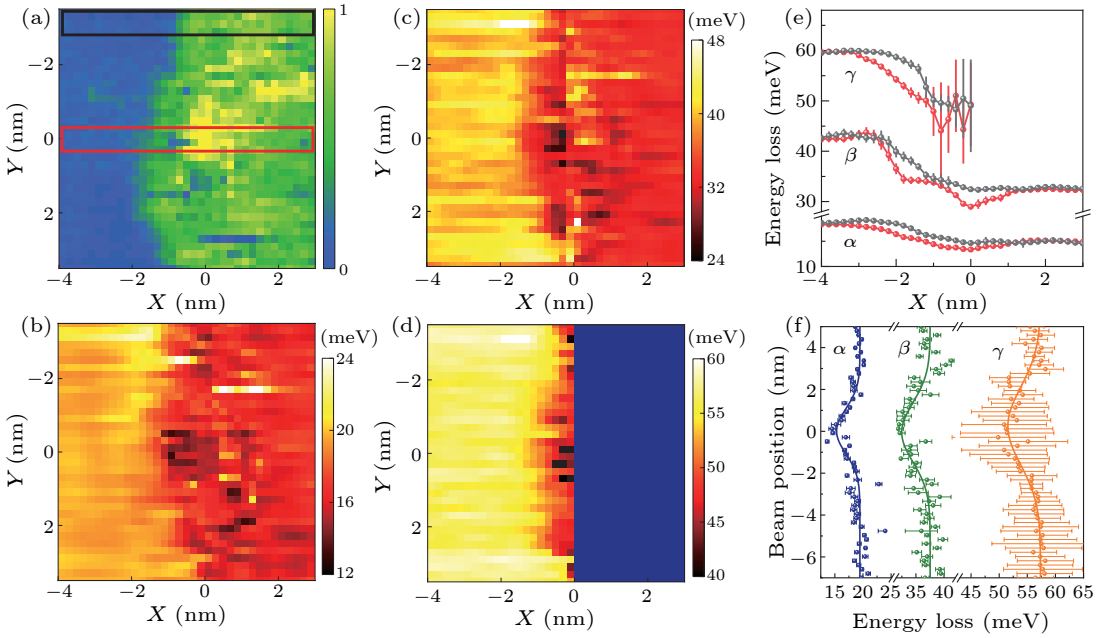

Fig. 2. The intensity and energy distribution maps of phonons. (a) The energy-filtered EELS intensity map of 6–14 meV window corresponding to one branch of the dislocation phonon modes. (b)–(d) The energy distribution maps of α, β, and γ phonon branches. The phonon energy is extracted by a simple Gaussian peak fitting model, all of them showing lower energy at the dislocation. (e) The line profiles of α, β, and γ phonon energy through the mixing layer (black) and interface dislocation (red) along the X direction denoted by solid rectangles in (a). (f) The data points of the phonon energy of α, β, and γ modes through the dislocation core along the Y direction denoted by rectangles in Fig. S5 of the SM. The solid lines are the fitted Gaussian distributions. The error bar is defined by the sum of standard deviations error and Gaussian fitting error; see Sec. 5 for more information.

phonons compared to the optical ones.[23] To verify the behavior of redshift and localization characteristics of dislocation phonons, frequency resolved frozen phonon multislice (FRFPMS)[45] simulations were also performed. Figure S6(a) of the SM shows the calculated scattering cross-section with the same experimental conditions (see details in the Sec. 5), while the energy filtered cross-section mappings are shown in Figs. S6(b)–S6(d) of the SM. The redshift of three peaks is well distinguishable, and the dislocation phonons are highly localized, which is in good agreement with the experimental data. Note that the phonon activity has been considered in this simulation, i.e., these local dislocation phonon modes in the simulation must be excitable by the electrons in this case.

4. MD Simulations and Thermal Transport Properties of the Si-Ge Interface. To further understand the origin of dislocation phonons and their effects on thermal transport properties, MD simulations are performed. Figure 3(a) shows the calculated PPDOS of Ge single crystal without (black) and with (red) an edge dislocation, respectively. Such an edge dislocation produces complex strain fields nearby, as illustrated by the experimental strain maps (Fig. S7 of the SM). Based on simulations in Fig. 3(a), the tensile strain region (the third layer) shows a redshift of α_{disl} and β_{disl} (as well as the redshift of γ_{disl} modes in Fig. S8), while the compressive strain region (the second layer) causes a blueshift of β_{disl} and γ_{disl} instead. However, only a redshift is observed in our experiment. This discrepancy between calculation and experiment suggests that the strain condition is not the sole mechanism. Indeed, the significant element segregation at the dislocation core [as shown in Fig. 1(c)] should also play an important role. At the Si side with compressive strain, the phonon energy is expected to blueshift, but the significant Ge segregation [as shown in Fig. 1(c)] at the dislocation core tends to make the phonon redshift, as the presence of heavier Ge atoms can lower the phonon energies. In this sense, the phonons at the dislocation rely on the competition between lattice disorder and element disorder. Apparently, the Ge segregation is dominant at the Si side. This is also validated by the experimental decoupling of the element segregation and strain contribution to the energy shift; the details are illustrated in Fig. S9 of the SM.

Now we discuss how the thermal transport properties are influenced by the dislocation and interface disorder layer with the aid of simulations. In general, the dislocations in a single crystal can cause a reduction in the phonon group velocity[46] and an increase in the anharmonic phonon-phonon scattering.[47] Both effects lead to the reduction of ITC,[12] which is beneficial for the enhancement of thermoelectric performance. For example, a previous study reported that the scattering of a wide spectrum of phonons by dislocations, grain boundaries, and other imperfections in SiGe alloys leads to a significantly low thermal conductivity of ∼0.93 W/(m·K), and thus enhances the thermoelectric figure of merit ∼1.84 at 1073 K.[48] In fact, besides SiGe alloys, dislocations were also introduced into many other thermoelectric materials to achieve high performance.[49,50]

However, the case for the dislocation at a heteroint-

erface, as studied here, is more complicated. It should be noted that the mixing layer plays an important role in the phonon transport across a heterointerface. Previous studies reported the existence of localized interfacial phonon modes at the Si/Ge interface, having a significant contribution to the ITC.[27] Since there exists significant phonon mismatch, many phonons (particularly those of optical phonons in Si) necessitate energy transfer to the other side through inelastic scattering processes, in which the localized interfacial phonon modes play a facilitating role. The inelastic scattering redistributes thermal energy among phonons through non-equilibrium effects induced by the heterojunction.[51,52] With the mixing layer, our study indicates that the low-frequency phonon modes surrounding α and β peaks act as bridges to connect the mismatch in phonon energy at the interface,[29,42,53] as shown in Fig. 2(e), which is beneficial to increase the ITC. In our practical case with both dislocation and interdiffusion at the interface, the effects of dislocation on thermal transport contain not only their competitions but also their interactions. To quantify the effect of these factors, we calculate the room-temperature lattice thermal conductivity (κ) of different structures with and without the inclusion of dislocation and interdiffusion, whose corresponding spectral thermal conductivities are shown in Figs. 3(c)–3(f). For comparison, the case of the pure Ge single crystal is also given. From Fig. 3(c), the dislocation in the pure Ge single crystal reduces its κ, as broadly seen in other single crystal systems.[47,54] For the Si/Ge interface without a mixing layer, the dislocation leads to an increase in κ instead. As for the interface with intermixing, the change in thermal conductivity is quite complicated, highly depending on the elemental distribution at the interface [the corresponding atomic models are shown in Fig. 3(b) and Fig. S10 of the SM]. The presence of dislocation increases κ in the case with the most significant interdiffusion (50% element mixing) but reduces κ in the case with Ge segregation in the dislocation core in our case.

The interfacial thermal transport behaviors above can be understood by examining the local PhDOS near the interface. Generally, the number of heat channels across an interface is closely related to the PhDOS overlap between the two sides of the interface according to the diffuse mismatch model, i.e., the higher (lower) the PhDOS overlap, the more (less) phonon transport channels.[53] The dislocation in pure Ge single crystal causes the vibrational mismatch of its surrounding atoms, thereby suppressing its κ in a wide frequency range [Fig. 3(d)]. For the Si/Ge interface without a mixing layer, the dislocation induces the redshift of phonons near the interface, which can weaken

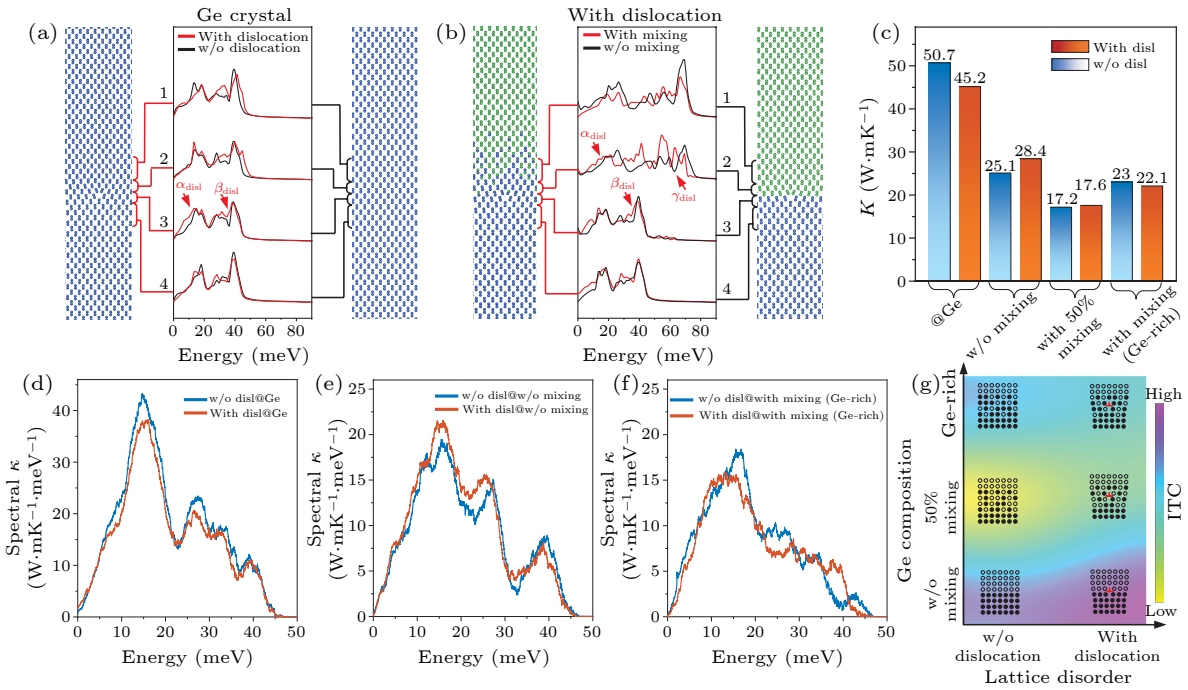

Fig. 3. MD simulations of different Si/Ge systems. (a) Schematic diagrams and calculated PhDOS of Ge crystal. Each layer is the PhDOS of the atoms covered by the brace. The dislocation modes β_{disl} (the red arrow) experience a redshift compared to the dislocation-free case (black). (b) Schematic diagrams and calculated PhDOS of Si/Ge systems with a dislocation. The dislocation modes show redshift at the intermixing region. (c) The dislocation effect on thermal conductivity in Ge, Si/Ge without a mixing layer, Si/Ge with a 50% intermixing layer, and Si/Ge with significant Ge segregation. Although in a single crystal Ge, the dislocation reduces the ITC, at the Si/Ge interface, the dislocations (orange) can either enhance or reduce the ITC compared to the dislocation-free case (blue). (d) The spectral thermal conductivity of Ge in the case of with dislocation (orange) and without dislocation (blue). (e) The spectral thermal conductivity of Si/Ge system without a mixing layer. (f) The spectral thermal conductivity of the Si/Ge system with a mixing layer (in a Ge-rich case). (g) Schematic diagram of the competitive relationship between dislocations and elemental mixing.

the vibrational mismatch caused by the heterointerface, i.e., increase the PhDOS overlap, as listed in Table S1 of the SM, thus giving rise to the increased contribution of mid- and low-frequency phonons (0–27 meV) [Fig. 3(e)]. When elemental interdiffusion is introduced into the interface, the element disorder bridges the PhDOS between the two sides of the heterointerface and thus increases the PhDOS overlap. For the case of significant Ge segregation in particular, the interface effects are severely diminished by the element disorder. In this case, the effect of introducing dislocations is similar to the single crystal case, which enables the suppression of κ in a wide frequency range as confirmed in Fig. 3(f). Figure 3(g) qualitatively illustrates the competitive relationship between dislocations and elemental mixing, where yellow (purple) hues indicate lower (higher) ITC. For the Si/Ge interface without a mixing layer, where there is a significant phonon energy mismatch between the two sides, dislocations can enhance inelastic phonon scattering, thereby improving ITC. However, when elemental mixing is introduced at the interface, the phonon energy difference between the two sides decreases, weakening the promoting effect of dislocations on inelastic phonon scattering and reducing the extent of ITC enhancement. When the interface contains a high concentration of Ge, the system more closely resembles a single crystal, with minimal phonon energy difference across the dislocation. In this case, the elastic scattering of phonons by dislocations becomes dominant, leading to a reduction in ITC.

5. Materials and Methods.

5.1. TEM Sample Preparation. The cross-sectional TEM specimen was prepared by mechanical polishing followed by argon ion milling carried out using the Precision Ion Polishing System (Model 691, Gatan Inc.). The specimen was baked at 160 ℃ for 16 hours to further remove the surface amorphous layer before EELS experiments.

5.2. Experimental Setup. The vibrational spectra were acquired at a Nion U-HERMES200 electron microscope equipped with both the monochromator and the aberration corrector, operated at 60 kV. The convergence semi-angle and the collection semi-angle were both 25 mrad. The electron beam was moved off the optical axis by approximately 50 mrad for off-axis experiments.[40] The scattering geometry and diffraction disks are shown in Fig. S11 of the SM. The energy dispersion channel was set to 0.5 meV with 2048 channels in total.

To exclude the possible effects from diffraction effects, slit aberration, and aperture charging, etc., on the signal below 20 meV, a set of 2D-EELS images was collected near the interface (Fig. S12 of the SM). The 2D-EELS data were collected under the same experimental conditions as in Fig. 1(d), i.e., the convergence semi-angle and the collection semi-angle were 25 mrad. The beam was shifted ∼50 mrad (off-axis) along the interface.

5.3. DFPT Simulations. The PhDOS were calculated using density functional perturbation theory by Quantum ESPRESSO.[55] The ultra-soft pseudopotential (USPP)[56] and the Perdew–Burke–Ernzerhof for solids (PBEsol)[57] exchange-correlation functional were used. The kinetic energy cut-off was 50 Rydbergs (Ry) for wavefunctions and 500 Ry for charge density and potential. The phonon dispersion and PhDOS were calculated by interpolating the dynamical matrix on an $8 \times 8 \times 8$ q-mesh.

5.4. MD Simulations. The MD simulations were performed using the large-scale atomic/molecular massively parallel simulator (LAMMPS) package[58] with a velocity Verlet algorithm for numerical integration of the equations of motion and a time step of 1 fs. All the interatomic interactions were described by the Stillinger–Weber potential.[59,60] The simulation systems contain $100\times10\times2$ conventional cells on both Si and Ge sides. Periodic boundary conditions were applied in all directions. To create the random atomic mixing layer, we selected the 4-unit-cell-long Ge layer near the interface and randomly replaced several Ge atoms with Si atoms. We generated a series of interface configurations with a random atomic mixing layer and obtained the most energetically stable atomic configuration by simulating the anneal-to-quench process from 1000 to 300 K. Our simulations were carried out in three steps. First, we performed simulations at 300 K and zero pressure in the isothermal-isobaric (NPT) ensemble using the Nosé/Hoover thermostat for 50 ps to help the system reach thermal equilibrium. Then the simulations were switched to the micro-canonical (NVE) ensemble for a further 50 ps to calculate the velocity autocorrelation function (VACF). Finally, nonequilibrium molecular dynamics (NEMD) simulations were conducted to calculate the thermal conductivities of six simulation systems for another 200 ps in the NVE ensemble, which is long enough to bring the systems to the stationary state and obtain the corresponding heat flux (J) and temperature gradient along the x direction (∇T). A fixed boundary condition is applied along the heat flow direction to eliminate direct thermal coupling between the heat source and sink regions. The temperatures at the source and sink regions of the simulation domains were controlled with Langevin thermostats.[61,62] Figure S13 in the SM shows the temperature profiles of NEMD simulations and the accumulated heat of the heat source domain and heat sink domain varying as a function of the simulation time.

The PhDOS was calculated by the fast Fourier transformation of VACF. The PhDOS projected on atom j can be calculated,

$$g_j(\omega) = \int \mathrm{e}^{\mathrm{i}\omega t} \frac{\langle v_j(t) v_j(0)\rangle}{\langle v(0) v(0)\rangle} \mathrm{d}t,$$

where ω is the phonon frequency, v_j is the velocity of atom j, and the $\langle \cdots \rangle$ brackets indicate averaging over different starting steps along the trajectory. The entire simulation domain was divided into many cells, and the PhDOS contributed by the atoms of each cell was calculated. According to Fourier's law, the lattice thermal conductivity (κ) is expressed as

$$\kappa = -\frac{J}{\nabla T}.$$

To quantify the effects of dislocation and random atomic mixing on the thermal transport of Si/Ge systems, we also calculated the spectral thermal conductivity as

$$\kappa_{\mathrm{sp}}(\omega) = -\frac{q(\omega)}{A \nabla T},$$

where $q(\omega)$ is the frequency-dependent spectral heat current, and A is the cross-sectional area of the simulation domain. More computational details and the full expression for $q(\omega)$ are referred to in Refs. [52,62,63]. Note that herein the temperature gradient was directly calculated as $\Delta T/L$ with a temperature difference between thermal reservoirs of ΔT and the simulation domain length of L, which has been demonstrated to be effective and reliable in computing κ.[64]

5.5. FRFPMS Simulations. Frequency resolved frozen phonon multislice method proposed by Zeiger *et al.*[45] was performed to verify whether the local modes near the dislocation can be excited by the electron beam. A model of $8\,\text{nm} \times 16\,\text{nm} \times 0.8\,\text{nm}$ with the same dislocation structure used in thermal properties calculations was used to calculate the local vibration spectrum. The system was fully relaxed under the NPT ensemble and then in the NVE ensemble. A 100 ps length NVE trajectory with a sample interval of 20 fs was used to calculate the band filtered trajectory. We performed Fast Fourier Transformation (FFT) on NVE MD trajectories in the time domain, then filtered trajectories with a 1 THz width Gaussian window-based bandpass filter with different central vibrational frequencies to achieve mode-specific refinement. This explicit parameterization (window function type, bandwidth magnitude) constitutes our unique spectral refinement strategy within the broader bandpass filtering framework. The frozen phonon multislice calculations were performed using the MD Frozen Phonon module embedded in the abTEM package[65] with a slice thickness of 0.2 nm. The statistical factor[66] of phonon population under 300 K is multiplied to suppress the excessively strong phonon signal under 20 meV.[67,68] A 10 meV width Gaussian was convoluted to smooth the spectra, and a 3 meV width Gaussian was used in the spectrum image to guarantee the visibility of localized phonon modes.

5.6. Phonon EELS Processing. The phonon EELS is firstly normalized by the integral of ZLPs, aligned using the cross-correlation method, and then denoised using the BM3D algorithm.[69] For background subtraction, the ZLPs are fitted using the Pearson VII function[70] with the energy window of $[-6, 6]$ meV and $[79, 99]$ meV. The function of Pearson VII is shown as

$$I(2\theta) = I_{\max}\frac{w^{2m}}{[w^2 + (2^{1/m} - 1)(2\theta - 2\theta_0)^2]^m},$$

where $I_{\max}$ is the peak value, w is the width of the peak, and m is the shape factor. The peak becomes a Lorentzian while $m \to 1$ and a Gaussian when $m \to 0$. The typical full width at half maximum (FWHM) of the fitted ZLP is $\sim$20 meV.

The ZLP subtracted data is then fitted using three Gaussian peaks with the fitting window of $[10, 30]$ meV for the α-peak, $[20, 50]$ meV for the β-peak, and $[30, 70]$ meV for the γ-peak. Figure S14(a) in the SM shows the multi-Gaussian fitting results of the EEL spectra acquired at different positions, and Figs. S14(b)–S14(d) show the standard deviation error, the Gaussian fitting error, and their combined uncertainty for peak fitting of phonon energies related to Fig. 2. While we note that the Gaussian fitting error is non-negligible, the characteristic redshift of the γ peak remains clearly resolvable and statistically significant. This observation is robust against the fitting uncertainties, as confirmed by our error analysis.

5.7. Core-Loss EELS Processing. The Si and Ge elemental maps can be extracted from the Si-K edge and the Ge-L edge of core-loss EELS. The background baselines of core-loss EELS are subtracted using the power law with the fitting window of $[1430, 1860]$ eV for Si and $[1120, 1200]$ eV for Ge. To extract the Si and Ge elemental maps, the energy windows for intensity integral on EELS are $[1871.0, 1890.6]$ eV for the Si-K edge and $[1116.4, 1402.1]$ eV for the Ge-L edge.

5.8. GPA Analysis. The geometry phase analysis (GPA) was performed by FRWRtools in DigitalMicrograph software, based on the work done by Hytch *et al.*[71] The FRWRtools is available from https://www.physics.hu-berlin.de/en/sem.

6. Conclusion. In summary, we directly measure the localized phonon modes of dislocations at the Si/Ge interface using atomic resolution STEM-EELS and reveal the effects on local thermal conductivity with the aid of MD simulations. Dislocations induce highly localized phonon modes within two nanometers of the core, exhibiting a redshift of several milli-electron-volts, which is lower than those in bulk Si and Ge. The competition between strain and element segregation accounts for the energy shift. Notably, the dislocation influences thermal transport in a complex manner, i.e., depending on the degree of element disorder, the local ITC could be either enhanced or reduced with the presence of dislocations, indicating intricate interactions between lattice disorder (structural discontinuities) and element disorder (compositional heterogeneity). These findings provide useful information to modulate thermal properties via defect engineering.

Acknowledgments. This work was supported by the National Natural Science Foundation of China (Grant No. 52125307) and the National Key R&D Program of China (Grant No. 2021YFB3501500). P.G. acknowledges the support from the New Cornerstone Science Foundation through the XPLORER PRIZE. We thank the helpful discussion with Prof. Jiaqing He at Southern University of Science and Technology (China) and Prof. Eric Stach at University of Pennsylvania (USA). We acknowledge the Electron Microscopy Laboratory of Peking University for the use of electron microscopes. We acknowledge the High-performance Computing Platform of Peking University for providing computational resources for simulations.

References

[1] Qian X, Zhou J, and Chen G 2021 *Nat. Mater.* **20** 1188
[2] Simoncelli M, Marzari N, and Mauri F 2019 *Nat. Phys.* **15** 809
[3] Luckyanova M N, Garg J, Esfarjani K *et al.* 2012 *Science* **338** 93
[4] Ravichandran J, Yadav A K, Cheaito R *et al.* 2014 *Nat. Mater.* **13** 168

[5] Poudel B, Hao Q, Ma Y *et al.* 2008 *Science* **320** 634
[6] Chen Z, Zhang X, and Pei Y 2018 *Adv. Mater.* **30** 1705617
[7] Chen J, Xu X, Zhou J, and Li B 2022 *Rev. Mod. Phys.* **94** 025002
[8] Polanco C A, Rastgarkafshgarkolaei R, Zhang J, Le N Q, Norris P M, and Ghosh A W 2017 *Phys. Rev. B* **95** 195303
[9] Tao Y, Wu C, Qi H, Liu C, Wu X, Hao M, Wei Z, Yang J, and Chen Y 2020 *Nanoscale* **12** 14838
[10] Gorham C S, Hattar K, Cheaito R *et al.* 2014 *Phys. Rev. B* **90** 024301
[11] Hopkins P E, Duda J C, Clark S P *et al.* 2011 *Appl. Phys. Lett.* **98** 161913
[12] Sun J, Li Y, Karaaslan Y, Sevik C, and Chen Y 2021 *J. Appl. Phys.* **130** 035301
[13] Chen Z, Ge B, Li W *et al.* 2017 *Nat. Commun.* **8** 1
[14] Wu Y, Nan P, Chen Z *et al.* 2020 *Adv. Sci.* **7** 1902628
[15] Gao P, Yang S, Ishikawa R *et al.* 2018 *Phys. Rev. Lett.* **120** 267601
[16] Krivanek O L, Lovejoy T C, Dellby N *et al.* 2014 *Nature* **514** 209
[17] Lagos M J, Trügler A, Hohenester U, and Batson P E 2017 *Nature* **543** 529
[18] Hage F S, Kepaptsoglou D M, Ramasse Q M, and Allen L J 2019 *Phys. Rev. Lett.* **122** 016103
[19] Venkatraman K, Levin B D A, March K, Rez P, and Crozier P A 2019 *Nat. Phys.* **15** 1237
[20] Huang S, Shi R, Li Y *et al.* 2021 *J. Vac. Sci. Technol* **3** 213
[21] Hage F, Radtke G, Kepaptsoglou D, Lazzeri M, and Ramasse Q 2020 *Science* **367** 1124
[22] Tian X, Yan X, Varnavides G *et al.* 2021 *Sci. Adv.* **7** eabi6699
[23] Yan X, Liu C, Gadre C A *et al.* 2021 *Nature* **589** 65
[24] Qi R, Shi R, Li Y *et al.* 2021 *Nature* **599** 399
[25] Gadre C A, Yan X, Song Q *et al.* 2022 *Nature* **606** 292
[26] Xu M, Bao D L, Li A *et al.* 2023 *Nat. Mater.* **22** 612
[27] Cheng Z, Li R, Yan X *et al.* 2021 *Nat. Commun.* **12** 6901
[28] Hoglund E R, Bao D L, O'Hara A *et al.* 2022 *Nature* **601** 556
[29] Li Y H, Qi R S, Shi R C *et al.* 2022 *Proc. Natl. Acad. Sci. U.S.A.* **119** e2117027119
[30] Haas B, Boland T M, Elsasser C *et al.* 2023 *Nano Lett.* **23** 5975
[31] Hoglund E R, Bao D L, O'Hara A *et al.* 2023 *Adv. Mater.* **35** e2208920
[32] Yan J, Shi R, Wei J *et al.* 2024 *Nano Lett.* **24** 3323
[33] Basu R and Singh A 2021 *Mater. Today Phys.* **21** 100468
[34] Schierning G 2014 *Phys. Status Solidi A* **211** 1235
[35] Su Y, Lu J, Villaroman D, Li D, and Huang B 2018 *Nano Energy* **48** 202
[36] Wood C 1988 *Rep. Prog. Phys.* **51** 459
[37] Hochbaum A I, Chen R, Delgado R D *et al.* 2008 *Nature* **451** 163
[38] Lee S M, Cahill D G, and Venkatasubramanian R 1997 *Appl. Phys. Lett.* **70** 2957
[39] Bathula S, Jayasimhadri M, Gahtori B *et al.* 2015 *Nanoscale* **7** 12474
[40] Dwyer C, Aoki T, Rez P, Chang S L Y, Lovejoy T C, and Krivanek O L 2016 *Phys. Rev. Lett.* **117** 256101
[41] Wei S and Chou M Y 1994 *Phys. Rev. B* **50** 2221
[42] Tian Z, Esfarjani K, and Chen G 2012 *Phys. Rev. B* **86** 235304
[43] Rez P and Singh A 2021 *Ultramicroscopy* **220** 113162
[44] Dwyer C and Etheridge J 2003 *Ultramicroscopy* **96** 343
[45] Zeiger P M and Rusz J 2020 *Phys. Rev. Lett.* **124** 025501
[46] Li M, Ding Z, Meng Q *et al.* 2017 *Nano lett.* **17** 1587
[47] Ni Y, Xiong S, Volz S, and Dumitrică T 2014 *Phys. Rev. Lett.* **113** 124301
[48] Basu R, Bhattacharya S, Bhatt R *et al.* 2014 *J. Mater. Chem. A* **2** 6922
[49] Shi X L, Zou J, and Chen Z G 2020 *Chem. Rev.* **120** 7399
[50] Mao J, Liu Z, Zhou J *et al.* 2018 *Adv. Phys.* **67** 69
[51] Maassen J and Askarpour V 2018 *APL Mater.* **7** 013203
[52] Sääskilahti K, Oksanen J, Tulkki J, and Volz S 2014 *Phys. Rev. B* **90** 134312
[53] English T S, Duda J C, Smoyer J L, Jordan D A, Norris P M, and Zhigilei L V 2012 *Phys. Rev. B* **85** 035438
[54] Wang T, Carrete J, Mingo N, and Madsen G K H 2019 *ACS Appl. Mater. Interfaces* **11** 8175
[55] Giannozzi P, Baroni S, Bonini N *et al.* 2009 *J. Phys.: Condens. Matter* **21** 395502
[56] Vanderbilt D 1990 *Phys. Rev. B* **41** 7892
[57] Perdew J P, Ruzsinszky A, Csonka G I *et al.* 2008 *Phys. Rev. Lett.* **100** 136406
[58] Plimpton S 1995 *J. Comput. Phys.* **7** 1
[59] Ding K and Andersen H C 1986 *Phys. Rev. B* **34** 6987
[60] Stillinger F H and Weber T A 1985 *Phys. Rev. B* **31** 5262
[61] Yang X, Carrete J, and Wang Z 2015 *J. Appl. Phys.* **118** 085701
[62] Yang X and Li W 2018 *Phys. Rev. Mater.* **2** 015401
[63] Sääskilahti K, Oksanen J, Volz S, and Tulkki J 2015 *Phys. Rev. B* **91** 115426
[64] Gu X, Fan Z, and Bao H 2021 *J. Appl. Phys.* **130** 210902
[65] Madsen J and Susi T 2021 *Open Res. Eur.* **21** 24
[66] Batson P E and Lagos M J 2018 *Microsc. Microanal.* **24** 412
[67] Zeiger P M and Rusz J 2021 *Phys. Rev. B* **104** 104301
[68] Zeiger P M, Barthel J, Allen L J, and Rusz J 2023 *Phys. Rev. B* **108** 094309
[69] Dabov K, Foi A, Katkovnik V, and Egiazarian K 2007 *IEEE Trans. Image Process.* **16** 2080
[70] Levin B D A, Venkatraman K, Haiber D M, March K, and Crozier P A 2019 *Microsc. Microanal.* **25** 674
[71] Hÿtch M J, Snoeck E, and Kilaas R 1998 *Ultramicroscopy* **74** 131